Structure of turbulent channel flow subjected to simultaneous inlet turbulence and localized injection

Masoud Asadi ⬤, Md. Kamruzzaman, and R. Jason Hearst ⬤[*]
Norwegian University of Science and Technology, Department of
Energy and Process Engineering, NO-7491 Trondheim, Norway

The combined effects of inlet turbulence and localized injection on turbulent channel flow are investigated experimentally in an air channel. A porous plate was used to locally inject air streams at the bottom wall of the channel, while an active grid at the inlet of the channel generated different inlet turbulence intensities. Six different wall boundary conditions as well as four different inlet turbulence cases were investigated with planar particle image velocimetry measurements above the injection zone and farther downstream of it. The results show that, above the injection zone, the mean velocity and all Reynolds stress components are significantly altered by the localized injection forming an affected layer (AL), while the inlet turbulence only intensifies the streamwise fluctuations. The AL is then transported away from the wall, and the results indicate that the inlet turbulence slightly facilitates this process by increasing the turbulence transport inside the channel. The measurement results at the downstream position show that the effects of the injection are still present in the flow; however, the AL is transported farther away from the wall to the outer layer. Turbulence structure analysis reveals that the inlet turbulence effects, such as amplifying intense streamwise fluctuations and increasing the contributions of different quadrant events to the total Reynolds shear stress, are more prominent in the central regions of the channel. On the other hand, above the injection zone, the localized injection was found to significantly affect the distribution of the fluctuations and quadrant contributions in the near-wall regions. The same effects, although less prominent, are still present at the downstream position yet only in the outer layer. Also, the inlet turbulence does not affect the inclined features of the internal boundary layer, while the localized injection slightly increases their inclination angle.

I. INTRODUCTION

Localized injection/blowing affects the structure of a boundary layer, causing severe deviations from its canonical state. Boundary layers with localized wall injection have thus been a topic of frequent investigation due to their prevalence in both nature and industrial applications. These investigations have been both experimental and numerical in nature and have been performed in various contexts, e.g., water seepage into a river from permeable bottom beds (e.g., Refs. [1–5]), skin friction reduction (e.g., Refs. [6–9]), as well as general studies of turbulent flow characteristics (e.g.,

―――――――

[*]jason.hearst@ntnu.no

Refs. [10–19]). Generally, injection is found to decrease the friction velocity (U_τ) of the boundary layer and amplify the Reynolds stresses.

Krogstad and Kourakine [14] used a porous strip to inject streams of fluid into a zero-pressure-gradient turbulent boundary layer (ZPG-TBL) at $\mathrm{Re}_\tau \approx 500$, where $\mathrm{Re}_\tau = U_\tau \delta_0 / \nu$ is the friction Reynolds number based on U_τ, the boundary layer thickness for the zero-injection case (δ_0), and kinematic viscosity of fluid (ν). Krogstad and Kourakine [14] tested four different blowing rates by performing cross-wire measurements at the center of the porous strip and several streamwise locations downstream of the injection strip. Above the injection plate, they observed strong effects of injection on the near-wall structure of the boundary layer, such as a reduction in the mean streamwise velocity, a decrease in local U_τ, and increased Reynolds stresses. They argued that the injection affects the flow across a limited range in the wall-normal direction, located in the near-wall region above the injection plate. When the flow passes the injection plate, the viscous sublayer immediately reforms, causing recovery of U_τ. The inner layer of fluid affected by the injection grows upward; therefore, downstream of the injection strip, the velocity deficit and the increased Reynolds stress regions are located farther from the wall. Krogstad and Kourakine [14] stated that the effects of injection were identifiable over the entire investigated range (up to $\sim 22\delta_0$ downstream of the injection strip). These observations were confirmed by later studies in a channel flow configuration [17,18]. Krogstad and Kourakine [14] also performed quadrant analysis using the hole filtering method [20], showing that contributions of the various quadrant events are also altered as a result of the injection.

Haddad *et al.* [18] investigated the effects of localized injection on the turbulence structure of a turbulent channel flow at $\mathrm{Re}_\tau \approx 250$, performing hot-wire measurements at two locations downstream of the injection plate. The authors did not perform any measurements directly above the injection chamber. Their results showed similar effects to the ones observed previously by Krogstad and Kourakine [14], such as increased Reynolds stress levels and decreased mean streamwise velocity and U_τ. These effects decayed farther downstream, however, were still distinguishable at the last measurement station. Haddad *et al.* [18] also argued that the localized injection increases the inclination angle of the near-wall structures.

Nevertheless, in most real turbulent flows, the incoming flow is subjected to several disturbances and hence significantly differs from the canonical cases. This can be interpreted as increased turbulence intensities at the inlet of a channel or a turbulent freestream on top of a flat plate boundary layer. Effects of freestream turbulence (FST) on ZPG-TBLs have been studied in great detail using experimental methods across a wide range of Re_τ (e.g., Refs. [21–31]) and more recently using direct numerical simulation (DNS) (e.g., Refs. [32–35]). FST is generally known to increase U_τ of ZPG-TBLs and suppress the wake region of the mean velocity profile, while having limited effects on the log layer [21–23,26–28,31].

Performing particle image velocimetry (PIV) measurements, Dogan *et al.* [28] investigated the structure of a ZPG-TBL subjected to FST, arguing that increased FST intensities penetrate well into the boundary layer, elevating the normal Reynolds stresses as well as the Reynolds shear stress. They also investigated distributions of Reynolds stresses and stated that increasing the FST level mainly amplifies the intense events in the near-wall regions. Performing quadrant analysis, they argued that FST alters the contributions of different quadrants in the outer regions of a ZPG-TBL, yielding more similarities to a turbulent channel flow. Dogan *et al.* [28] also examined the two-point spatial correlations and found FST does not change the structural organization of the flow close to the wall. However, the correlations were shorter in space for the FST cases compared with canonical cases.

Despite various studies on ZPG-TBLs under the influence of a turbulent freestream, the impacts of inlet turbulence on turbulent channel flow are relatively unexplored. Asadi *et al.* [36] recently examined the influence of increased inlet turbulence intensities on the quiescent core and turbulence statistics of turbulent channel flow. They argued that, despite some similarities between this flow and ZPG-TBLs subjected to FST, e.g., a suppressed wake region, an intact log region in the velocity profile, and the increased streamwise fluctuations, there are also remarkable differences. Asadi *et al.*

[36] observed that, in contrast to the previous studies for a ZPG-TBL subjected to FST, increased inlet turbulence intensities did not affect U_τ, the Reynolds shear stress, and wall-normal velocity fluctuations of turbulent channel flow. Furthermore, increased inlet turbulence was found to strongly affect the momentum level of the quiescent core of turbulent channel flow, where it yielded high-momentum and low-momentum cores in addition to the conventional core of turbulent channel flow.

Although the previous studies were of great importance for understanding the characteristics of wall-bounded flows subjected to wall injection, in most practical applications, where the turbulent flow is subjected to wall injection, the inlet condition is far from the idealized canonical form. Thus, it is worth investigating the impacts of these two coexisting factors, i.e., localized injection and elevated inlet turbulence intensity, on the structure of turbulent channel flows. It should be mentioned that the combined effects of roughness and injection were studied previously by several scholars (e.g., Refs. [37–40]); nevertheless, study of a wall-bounded flow simultaneously subjected to increased incoming turbulence intensities and wall injection is lacking. Accordingly, in this paper, we seek to investigate the structure of a turbulent channel flow subjected to different localized injection rates and increased inlet turbulence levels. A porous plate was used to inject distributed streams into the flow; meanwhile, an active grid placed at the channel entrance was utilized to control the inlet flow conditions. Different injection rates and inlet turbulence intensities were examined using PIV measurements at two different streamwise locations, i.e., above the injection location and farther downstream of it. The turbulence statistics are reported as well as the results of turbulence structural analysis.

II. EXPERIMENT

A. Experimental setup

The air channel flow facility at the Norwegian University of Science and Technology was used to perform the experiments. The facility is the same as described by Asadi *et al.* [36], with an extra injection chamber added to locally inject distributed streams. The channel has a test section built out of acrylic, with a height ($H = 2h$) of 50 mm and a width (W) of 600 mm, providing an aspect ratio (W/H) of 12, high enough to prevent corner effects on the flow in the center of the channel [41–43]. The flow was produced by a centrifugal fan and passed through a series of straightener screens followed by a 48:1 contraction before reaching the test section inlet. An active grid was located at $X = 2.5H$ to manipulate inlet flow conditions (X is the streamwise coordinate system whose origin is located at the channel inlet). The grid consists of 12×2 rectangular space-filling wings that were three-dimensionally (3D) printed out of polylactic acid plastic (see Fig. 1(a) for a schematic). Each wing is directly connected to a stepper motor. The motors were actuated by random signals specifying the rotation direction, duration, and speed. Thin strips of multigrade grip tape were placed at $X = 3.5H$ to trip the boundary layers on the bottom and top of the channel. The test section extends $\sim 105H$ downstream of the trip. A pressure scanner (Scanivalve MPS4264 ± 4 inH$_2$O full-scale range) with a $\pm 2\%$ accuracy of the full scale was used to measure the pressure drop along the channel at 16 pressure taps spaced in intervals of 325 mm ($6.5H$) with the first tap located $7.5H$ downstream of the inlet. The mean shear stress (τ), hence the friction velocity (U_τ), was calculated by fitting a line to the mean pressure drop measured by the last 8 pressure taps. The linearity of the measured pressure drop resulted in R^2 values >0.998.

For the localized injection, a chamber was embedded in the bottom wall of the channel. A mass flow controller (Alicat MCR-3000SLPM), supplied by a pressurized air stream with a gauge pressure of 5 bar, was used to control the injection flow rates. The chamber was supplied through 6 inlet valves connected to the outlet of the mass flow controller. Figure 1(b) shows a schematic of the injection zone, where a porous plate (GKN Sinter Metals, SIKA-R5) was installed on top of the injection chamber, whose center was located $75H$ downstream of the inlet. The porous plate distributed the air stream across an area of 15 cm (streamwise) $\times$ 27.5 cm (spanwise), i.e., $6h \times 11h$. The plate was manufactured by cold isostatic pressing of stainless steel powder, excelling in uniform

(a)

87H

76H

Flow

2.5H

$H = 2h$

Active grid

Injection chamber

(b)

Camera

Laser sheet

12H

11h

6h

500 μm

76H from the inlet

(c)

Flow direction

12H

$H = 2h$

Porous plate
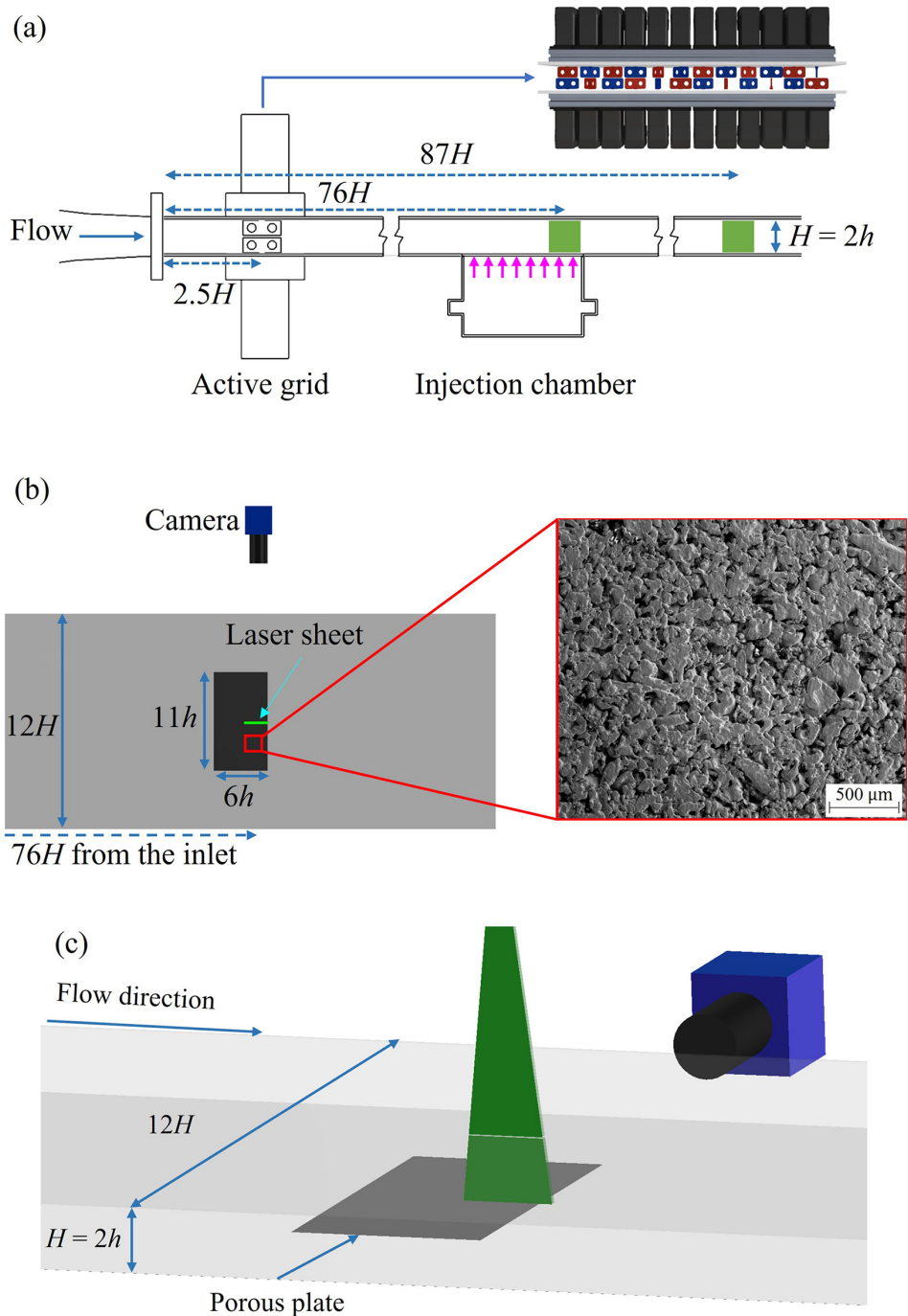
FIG. 1. Schematics of the setup. (a) Side view, where the interrogated regions are illustrated with green boxes, together with a snapshot of the frontal view of the active grid in a random rotational sequence. (b) Top view showing the configuration of the particle image velocimetry (PIV) setup for the measurements above the injection plate together with a scanning electron microscopy (SEM) image of the porous plate surface. (c) Three-dimensional (3D) view of the PIV setup for the measurements above the injection plate.

TABLE I. Active grid and flow parameters of the smooth wall test cases together with the RMSD of the mean velocity and turbulence intensity profiles between $X = 76H$ and $87H$.

Grid case	$\Omega \pm \omega$ (Hz)	U_τ (ms^{-1})	u'_0/U_0 (%)		RMSD (%)	
			76H	87H	U/U_0	u'/U_0
REF	Static	0.321	3.7	3.9	1.8	4.0
A	9.0 ± 3.0	0.325	4.8	4.6	2.3	2.5
B	4.5 ± 1.5	0.324	5.2	4.9	2.2	3.2
C	0.75 ± 0.25	0.324	6.6	6.0	2.5	6.2

porosity with homogeneous physical characteristics, which in turn ensures the uniformity of the injected streams. Figure 1(b) shows a magnified view of the porous plate surface captured by scanning electron microscopy (SEM). The surface roughness profile of the porous plate was obtained using white light interferometry. The results showed a maximum peak-to-trough height of 191 μm, i.e., $k_t^+ = U_\tau k_t/\nu \approx 4.1$, and a root mean square deviation of 26 μm, i.e., $k_{\mathrm{rms}}^+ = U_\tau k_{\mathrm{rms}}/\nu \approx 0.5$, which are small enough to neglect the roughness effects in the log region of the boundary layer [44]. This notion is also confirmed by the results presented in Sec. III.

B. Test cases

The inlet turbulence intensity was set by four different active grid cases, determined by the different sequences used to control the motors of the grid. One of the four was a static reference (REF) case where the wings were kept constant in their fully opened position. The other three were active cases with the same random sequences as used in the previous study [36] and listed in Table I. Here, Ω is the mean rotational velocity, and $\omega = \Omega/3$ is the limiting parameter of the top-hat distribution. The active cases are labeled A, B, and C in the order of increasing centerline turbulence intensity (u'_0/U_0, where u'_0 denotes the standard deviation of the centerline velocity and U_0 is the mean centerline velocity, both in the streamwise direction). The turbulence intensity was shown to have an inverse relation with the rotation speed of the wings, which is in line with previous studies [36,45,46]. Here, U_0 was kept constant at 6.7 m/s within $\pm 2\%$. The resulting Reynolds number (Re$_H$) based on U_0 and H was $\sim$22 300. Table I lists the U_τ values for smooth wall cases. It is evident that the inlet turbulence intensity does not considerably affect the friction velocity of channel flow for the turbulence levels tested here, resulting in a matched Re$_\tau \approx 535$; this agrees with our previous findings [36]. To assess the streamwise evolution of the flows, U/U_0 and u'/U_0 profiles of the smooth wall cases were compared between two measurement locations, $X/H = 76$ and 87. The profiles were interpolated on a common grid to quantify the discrepancies. The resulting root-mean-square differences (RMSDs), normalized by the downstream measurement results, are listed in Table I for these cases. Considering the distance between the two measurement locations, which is >20 boundary layer thicknesses ($>20h$), and relatively small changes in the statistics between the two measurement locations, especially when compared with the perturbations caused by the wall injection, the streamwise evolution is deemed to have negligible effects on the trends observed herein.

Six different bottom wall boundary conditions are considered at $73.5 < X/H < 76.5$. A smooth wall case (S) which was then replaced by the porous plate to impose the other 5 boundary conditions, i.e., a no-injection case (I0), and four different injection rates through the porous plate with blowing ratios of $V_i/U_0 = 0.1$, 0.6, 1.1, and 2.1% (V_i denotes the mean injection velocity at the wall), labeled as I1, I2, I3, and I4, respectively. These 6 cases were combined with 4 inlet turbulence cases, resulting in 24 different test cases, which were examined by PIV measurements at two different streamwise locations. Different measurement cases are coded α_β_γ, where α, β, and γ indicate the boundary condition, the inlet turbulence case, and the measurement location (X/H), respectively.

TABLE II. Flow parameters of all test cases at $X = 76H$ and $87H$ together with the PIV camera used for each test case. The test cases are coded as α_β here, for α and β indicating the boundary condition at the bottom wall and the inlet turbulence case, respectively. V_i denotes the mean injection velocity through the porous plate, and U_0 is the mean streamwise velocity at the channel centerline. u_0'/U_0 and v_0'/U_0 are centerline streamwise and wall-normal turbulence intensities, respectively.

| Case | V_i/U_0 (%) | PIV camera | | U_0 (ms^{-1}) | | u_0'/U_0 (%) | | v_0'/U_0 (%) | |
		76H	87H	76H	87H	76H	87H	76H	87H
S_REF	—	sCMOS	sCMOS	6.7	6.6	3.7	3.9	3.0	3.1
S_A	—	sCMOS	sCMOS	6.6	6.6	4.8	4.6	3.2	3.2
S_B	—	sCMOS	sCMOS	6.6	6.6	5.2	4.9	3.3	3.3
S_C	—	sCMOS	sCMOS	6.6	6.6	6.6	6.0	3.3	3.3
I0_REF	0	sCMOS	WX100	6.7	6.7	3.7	3.7	3.0	3.0
I0_A	0	sCMOS	WX100	6.6	6.7	4.9	4.5	3.3	3.0
I0_B	0	sCMOS	WX100	6.7	6.7	5.2	4.8	3.3	3.2
I0_C	0	sCMOS	WX100	6.6	6.7	6.6	5.8	3.3	3.1
I1_REF	0.1	sCMOS	WX100	6.7	6.7	3.8	3.8	3.0	3.0
I1_A	0.1	sCMOS	WX100	6.7	6.7	4.8	4.5	3.3	3.1
I1_B	0.1	sCMOS	WX100	6.7	6.7	5.3	4.8	3.3	3.1
I1_C	0.1	sCMOS	WX100	6.7	6.7	6.6	6.0	3.3	3.1
I2_REF	0.6	sCMOS	WX100	6.7	6.8	3.7	3.8	3.0	3.0
I2_A	0.6	sCMOS	WX100	6.7	6.7	4.9	4.5	3.2	3.1
I2_B	0.6	sCMOS	WX100	6.7	6.7	5.1	4.8	3.3	3.2
I2_C	0.6	sCMOS	WX100	6.7	6.7	6.6	5.9	3.3	3.2
I3_REF	1.1	sCMOS	WX100	6.7	6.7	3.8	4.0	3.0	3.1
I3_A	1.1	sCMOS	WX100	6.7	6.7	4.9	4.7	3.3	3.2
I3_B	1.1	sCMOS	WX100	6.7	6.7	5.1	4.9	3.4	3.3
I3_C	1.1	sCMOS	WX100	6.7	6.7	6.4	5.9	3.3	3.3
I4_REF	2.1	sCMOS	WX100	6.8	6.7	3.8	4.4	3.0	3.4
I4_A	2.1	sCMOS	WX100	6.8	6.7	4.8	5.1	3.2	3.4
I4_B	2.1	sCMOS	WX100	6.8	6.7	5.1	5.2	3.3	3.5
I4_C	2.1	sCMOS	WX100	6.8	6.7	6.3	6.4	3.3	3.5

More detailed flow parameters are provided in Table II. It should be mentioned that it was not feasible for the injection cases to estimate the friction velocity by measuring the pressure drop along the channel since strong streamwise gradients were present and the injection caused asymmetry.

C. PIV measurements

Planar PIV measurements were performed to investigate the flow features in the streamwise–wall-normal (x-y) plane in the center of the channel. The measurements were performed at two streamwise locations, $X/H = 76$ and 87, to explore the flow characteristics above the injection zone and the flow evolution farther downstream of it (Fig. 1). A Litron Nano L200-15 PIV laser (dual-pulse Nd : YAG) with a maximum energy of 200 mJ per pulse was used to generate a laser beam, which was then passed through the LaVision light sheet optics to produce a thin sheet. A LaVision Imager sCMOS camera (2560×2160 pixels, 16 bit) was fitted with a lens of focal length 100 mm (Zeiss Milvus 2/100M) to cover the full height of the channel ($2h$) and $\sim1.7h$ in the streamwise direction. Double-frame images were captured for the test cases labeled sCMOS in Table II. For the other cases (labeled WX100 in Table II), a Photron FASTCAM Mini WX100 (2048×2048 pixels, 12 bit) equipped with a lens of focal length 180 mm (Sigma F2.8 EX) was
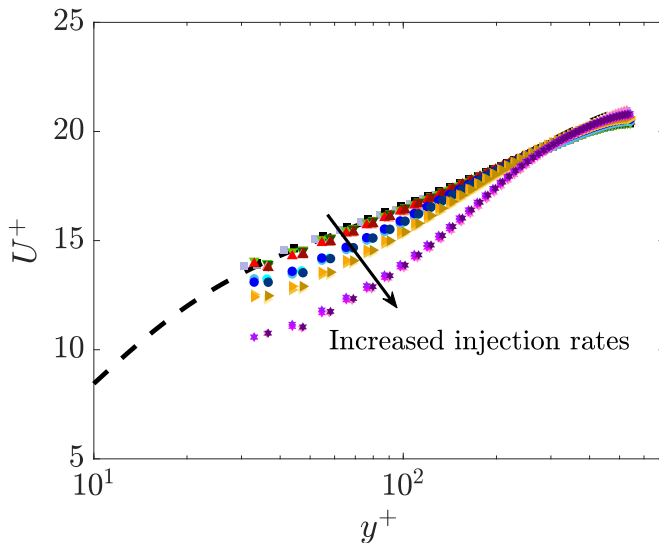
FIG. 2. Inner-normalized mean velocity profiles above the injection plate ($X = 76H$) for all test cases: S (■, gray), I0 (▼, green), I1 (▲, red), I2 (●, blue), I3(▶, yellow), and I4 (⋆, purple), with darkening colors indicating increased inlet turbulence intensity, i.e., REF, A, B, and C, respectively. The dashed black line indicates direct numerical simulation (DNS) data of turbulent channel flow at $\mathrm{Re}_\tau \approx 550$ [49].

utilized to capture double-frame images, covering a field of view that measured $\sim 2h$ in both the wall-normal and streamwise directions. It should be mentioned that using two different cameras was a result of practical constraints. All the image pairs were recorded and processed in LaVision DaVis 10.1, where a final pass window size of 48×48 pixels with an overlap of 75% in an iterative cross-correlation process was used, resulting in a spatial resolution of 25 viscous units (y^+) or better for all cases. The estimated uncertainties of the instantaneous velocities based on correlation methods [47,48] were $\sim 5\%$ of the centerline mean velocity in the regions close to the bottom wall of the channel and dropped to $<1\%$ away from the wall. As a precaution, the first and last 5 rows of the processed vector fields, i.e., close to the bottom and top walls, were disregarded throughout the analysis.

III. FIRST- AND SECOND-ORDER STATISTICS

To assess the combined influence of localized injection and inlet turbulence on the mean turbulence statistics, profiles of mean streamwise velocity as well as the turbulent fluctuations are plotted for different test cases. The profiles are inner-normalized by the U_τ values of the smooth wall cases listed in Table I to underline the effects of localized injection on the profiles. Section III A compares the mean streamwise velocity profiles of the different cases measured at two different streamwise locations. Subsequently, the profiles of different Reynolds stress components are illustrated in Sec. III B. DNS data of turbulent channel flow at $\mathrm{Re}_\tau \approx 550$ [49] are also included for comparison with the present $\mathrm{Re}_\tau \approx 535$ experimental data.

A. Streamwise mean velocity

Figure 2 shows the mean streamwise velocity profiles of all test cases measured at $X = 76H$, i.e., on top of the injection zone. The results indicate that the substitution of the smooth wall with the porous wall, due to the negligible roughness of the porous plate, i.e., $k_t^+ = 4.1$, does not considerably affect the mean velocity profiles. According to our previous observations [36], the
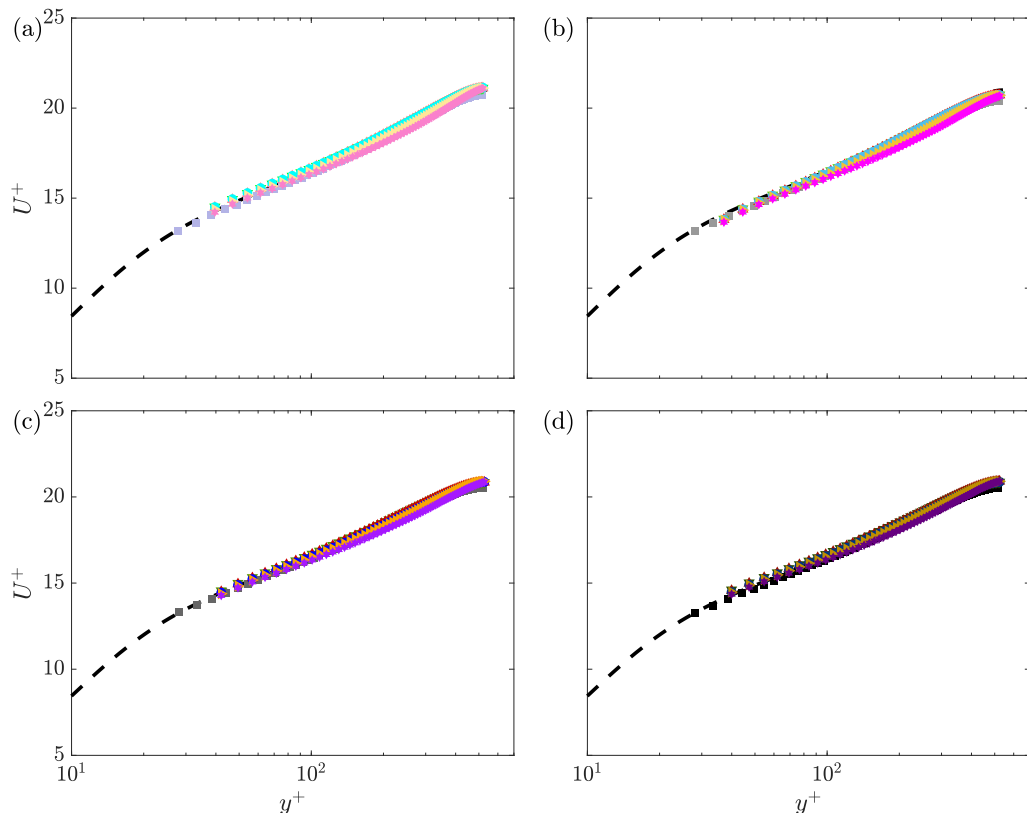
FIG. 3. Inner-normalized mean velocity profiles downstream of the injection plate ($X = 87H$) for cases (a) REF, (b) A, (c) B, and (d) C for S (■, gray), I0 (▼, green), I1 (▲, red), I2 (●, blue), I3(►, yellow), and I4 (★, purple). The dashed black lines indicate DNS data of turbulent channel flow at $\mathrm{Re}_\tau \approx 550$ [49].

inlet turbulence level did not affect the mean streamwise velocity profiles in the inner regions of the boundary layer, but it did suppress the wake region. The same effects are observed here, where the increased turbulence intensity is found to only have a minor wake suppression effect on the mean velocity profiles. On the other hand, the localized injection gives rise to a velocity-deficit region in the inner regions of the boundary layer. The velocity deficit is intensified by increased injection rates. The observed velocity deficit is like the previous observations for localized injection in a ZPG-TBL [14] and turbulent channel flow [18]. Inversely, a minor velocity-surplus region emerges in the central regions of the channel as compensation for the velocity defect. This occurs because the top boundary layer prevents a free adjustment of the lower boundary layer of the channel. Nonetheless, the location of the maximum mean velocity ($y_{\max}/h$) moves toward the side opposite the injection wall by ~5% above the injection plate ($X = 76H$) for I4 cases. In contrast, the velocity-surplus region does not exist in a ZPG-TBL affected by localized injection due to a free adjustment of the boundary layer thickness to compensate for the velocity deficit in the near-wall region. The reader is reminded here that the profiles are normalized by the reference U_τ values, i.e., smooth wall cases, to highlight the effects of localized injection. In fact, the injection locally decreases the friction velocity of the flow by decelerating it in the near-wall region; therefore, had the local U_τ values been used for normalization, the velocity profiles would have collapsed in the near-wall region, exhibiting discrepancies in the outer regions (see Krogstad and Kourakine [14], Fig. 3). It is worth mentioning that the localized injection initiates a sharp streamwise gradient which is not present in Fig. 2 due to
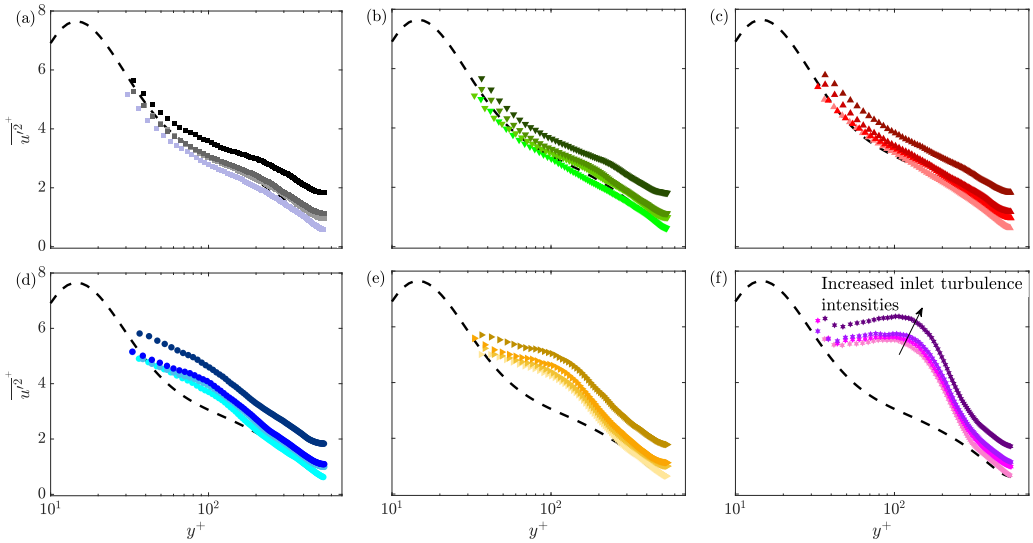
FIG. 4. Inner-normalized streamwise normal Reynolds stress profiles above the injection plate ($X = 76H$) for cases (a) S, (b) I0, (c) I1, (d) I2, (e) I3, and (f) I4 with darkening colors indicating increased inlet turbulence intensity, i.e., REF, A, B, and C, respectively. The dashed black lines indicate DNS data of turbulent channel flow at $\mathrm{Re}_\tau \approx 550$ [49].

the streamwise averaging of the velocity profiles across the PIV domain. This streamwise gradient is elaborated on in Appendix for the highest injection case I4.

Figure 3 presents the mean velocity profiles measured at $X = 87H$, which is located $22h$ downstream of the injection plate. The results show the recovery of the velocity profiles in the near-wall region, while the velocity-defect region is transported away from the wall. Hence, the prominent velocity deficit in the near-wall region disappears, and a weak velocity deficit appears at $200 \lesssim y^+ \lesssim 400$. The presence of the velocity defect region demonstrates the long-lasting effects of the localized injection $>20h$ downstream of the injection plate. In this location, for the cases with the highest injection rate, $y_{\max}/h$ was displaced $\sim 9\%$ toward the upper half of the channel. Once more, relative to the injection, the inlet turbulence intensity does not seem to play an important role except for a minor wake suppression effect.

B. Turbulent fluctuations

Figure 4 shows profiles of the streamwise fluctuations for different test cases with the same boundary conditions at the bottom wall. Like the results of our previous study [36], increasing the inlet turbulence intensity increases the streamwise fluctuations. Figures 4(b)–4(f) indicate that the amplification of the streamwise fluctuations occurs regardless of the bottom wall boundary condition. Furthermore, Fig. 5 presents the same profiles for cases REF and C with different bottom wall boundary conditions, demonstrating that the injection intensifies the fluctuations of the streamwise velocity in the inner regions of the boundary layer. As described by Krogstad and Kourakine [14], an extra sublayer is created by the localized injection across which the fluctuations are amplified. This sublayer is herein referred to as the *affected layer* (AL). For the highest injection rate, the amplifications are strong enough for the profiles to exhibit a second peak. Again, it should be mentioned that the streamwise evolution of the profiles that experience localized injection is not accounted for here, as the profiles are averaged in the streamwise direction. This is the reason that an approximately flat region emerges in the inner region ($50 \lesssim y^+ \lesssim 150$) of the profiles for the highest injection rates, i.e., I3 and I4 (see Appendix for details). In line with the
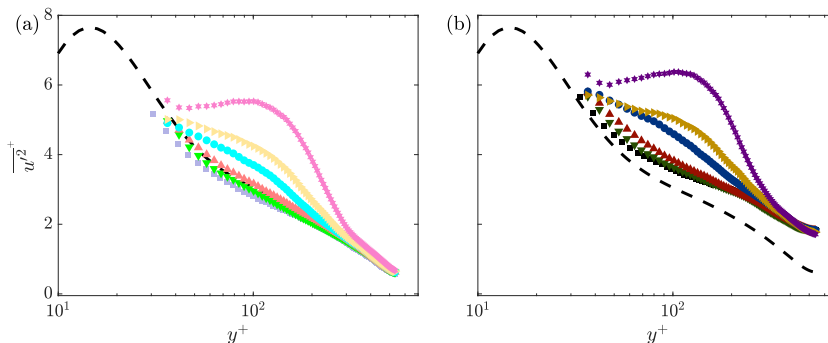
FIG. 5. Inner-normalized streamwise normal Reynolds stress profiles at $X = 76H$ for cases (a) REF, and (b) C for S (■, gray), I0 (▼, green), I1 (▲, red), I2 (●, blue), I3(▶, yellow), and I4 (★, purple). The dashed black lines indicate DNS data of turbulent channel flow at $\mathrm{Re}_\tau \approx 550$ [49].

observations for the mean velocity profiles, the porous wall boundary condition (green curves) did not considerably affect the streamwise fluctuations except for a minor amplification in the near-wall region which is deemed to be negligible considering the significant effects of the localized injection.

When considering the combined effects of localized injection and inlet turbulence, the increased inlet turbulence intensity enhances the transport of the injection induced AL away from the wall. This is evident in Figs. 4(e) and 4(f), where the variance profiles move up diagonally with increasing inlet turbulence intensity.

Figure 6 shows the streamwise fluctuation profiles at $X = 87H$ for cases REF and C, the extreme cases. The AL is now farther from the wall and mainly affects the same regions ($200 \lesssim y^+ \lesssim 400$) as observed for the mean velocity profiles (Fig. 3). Like the upstream position, the inlet turbulence effect of increasing the fluctuations of the streamwise velocity is ubiquitous across all cases regardless of the injection rate (the profiles are not shown here for brevity). Like the mean velocity profiles, it is evident that the effect of localized injection is still present in the flow far downstream of the injection zone. Nonetheless, the profiles match in the near-wall region. In fact, the viscous sublayer is quickly re-established downstream of the injection plate, while the AL is transported toward the outer layer. As a result, the near-wall region recovers, leaving the outer region affected by the AL [14].
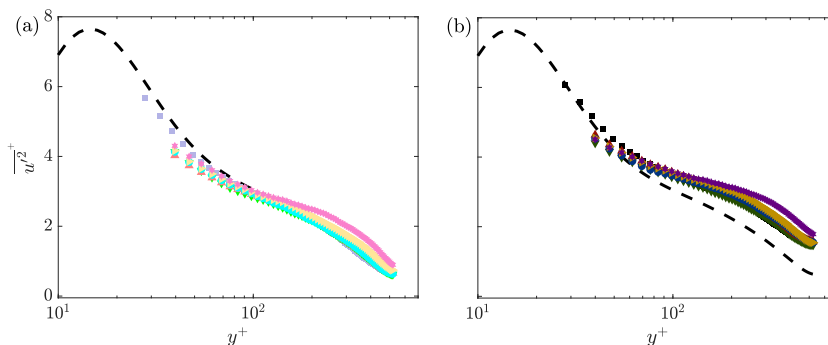
FIG. 6. Inner-normalized streamwise normal Reynolds stress profiles downstream of the injection plate ($X = 87H$) for cases (a) REF and (b) C for S (■, gray), I0 (▼, green), I1 (▲, red), I2 (●, blue), I3(▶, yellow), and I4 (★, purple). The dashed black lines indicate DNS data of turbulent channel flow at $\mathrm{Re}_\tau \approx 550$ [49].
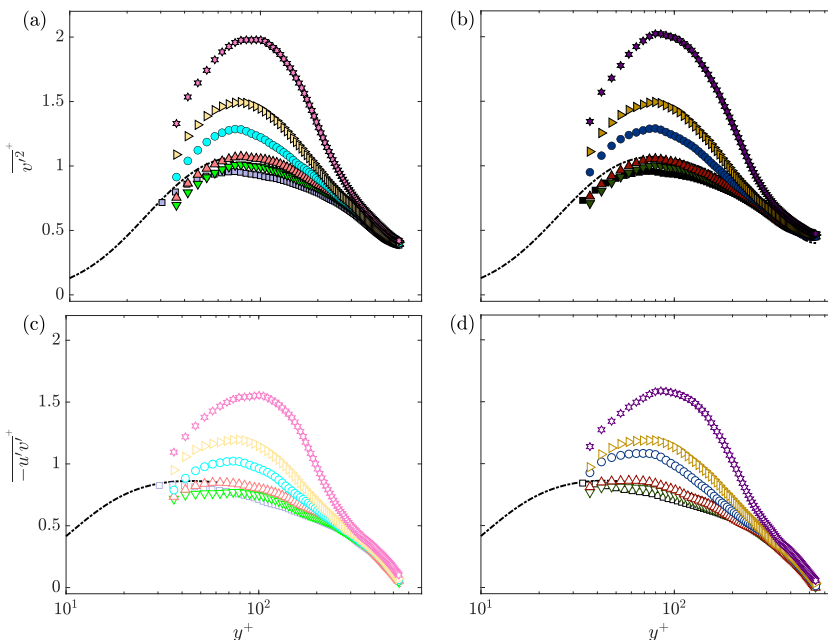
FIG. 7. Inner-normalized wall-normal Reynolds stress profiles for (a) REF and (b) C, and Reynolds shear stress profiles for (c) REF and (d) C above the injection plate ($X = 76H$) for S (■, gray), I0 (▼, green), I1 (▲, red), I2 (●, blue), I3(▶, yellow), and I4 (⋆, purple). The dashed black lines indicate DNS data of turbulent channel flow at $\mathrm{Re}_\tau \approx 550$ [49].

It was previously observed that increasing the inlet turbulence intensity of the turbulent channel flow does not considerably affect the wall-normal fluctuations and Reynolds shear stress [36]. The same result is observed for all cases tested in this paper. Figures 7 and 8 show the wall-normal fluctuations and Reynolds shear stress profiles for the two extreme cases REF and C to highlight the effect of localized injection. The injection, in contrast to the inlet turbulence intensity, substantially increases both the wall-normal fluctuations and Reynolds shear stress across the AL. The trends with increasing injection rate are the same as the ones mentioned earlier for the streamwise fluctuations. The intensified wall-normal and shear fluctuations explain the enhanced transport of the AL for increased injection rates. For reference, the wall-normal turbulence intensities at the centerline of the channel are listed in Table II for all test cases. The internal boundary layer turbulent statistics for increasing localized wall injection corroborate previous observations by Refs. [14,17,18]. In this paper, we have assessed this more rigorously in the context of increasing incoming turbulence, and the effects of the injection and inlet turbulence appear to be superimposed.

IV. ANALYSIS OF THE TURBULENCE STRUCTURE

In addition to investigating the effects of localized injection and inlet turbulence on the turbulent statistics, a detailed turbulence structure analysis is performed to further explore the effects on the structure of the internal boundary layer. Probability distribution functions (PDFs) of the fluctuating components are analyzed in Sec. IV A. Quadrant analysis is detailed in Sec. IV B, and velocity correlations are presented in Sec. IV C. The analyses were carried out for all test cases; however, for brevity, the results are shown here only for no injection and the highest injection (I0 and I4, respectively) with the lowest and highest inlet turbulence intensities
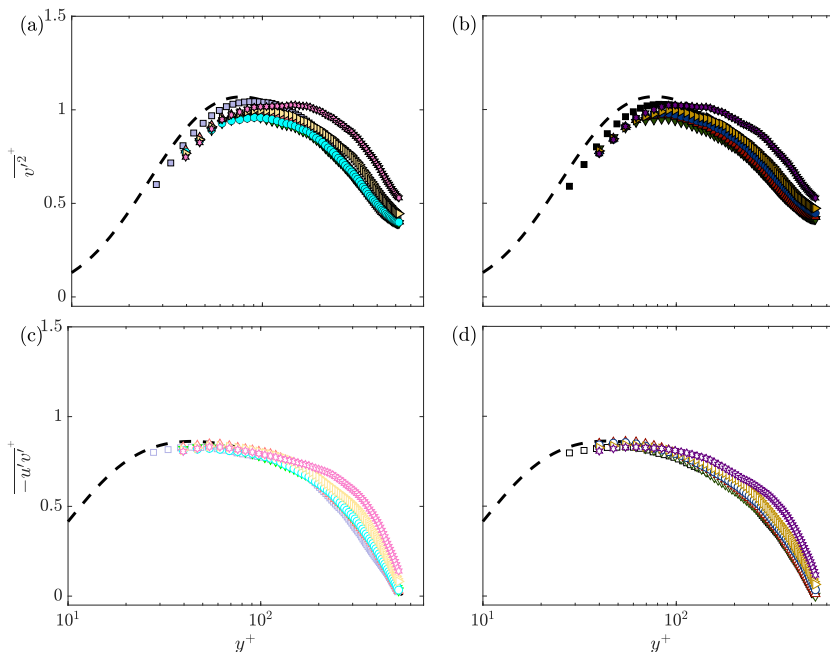
FIG. 8. Inner-normalized wall-normal Reynolds stress profiles for (a) REF and (b) C, and Reynolds shear stress profiles for (c) REF and (d) C downstream of the injection plate ($X = 87H$) for S (■, gray), I0 (▼, green), I1 (▲, red), I2 (●, blue), I3 (►, yellow), and I4 (⋆, purple). The dashed black lines indicate DNS data of turbulent channel flow at $Re_\tau \approx 550$ [49].

(REF and C, respectively) to highlight the effects of the localized injection and inlet turbulence intensity.

A. PDF analysis

PDFs of the Reynolds stresses at two wall-normal locations, i.e., $y^+ \approx 100$ and $y/h \approx 0.8$, are presented here to pinpoint the effects of localized injection and inlet turbulence on the inner and outer regions of the boundary layer, respectively.

Figure 9 shows the distributions of the normal Reynolds stresses as well as the Reynolds shear stress. Generally, the fluctuations are stronger in the inner layer, and the Reynolds shear stress distributions are skewed toward negative values, as is expected for a boundary layer. A close look at the I0 cases (green PDFs) underscores the fact that the inlet turbulence mainly boosts the streamwise velocity fluctuations. The increased inlet turbulence intensity elevates the streamwise fluctuations across the full range at $y/h \approx 0.8$ [Figs. 9(d) and 9(j)]. Although less prominent, some effects of inlet turbulence on the strong streamwise fluctuation events, i.e., the tail of the PDF, are observed in the inner layer [Figs. 9(a) and 9(g)], indicating that the penetration of the inlet turbulence into the boundary layer amplifies the extreme u' events. Conversely, the distributions of the wall-normal fluctuations appear to be independent of the inlet turbulence level tested in this paper at both wall-normal locations. Also, minor effects of the inlet turbulence on the positive Reynolds shear stress events are observed at $y/h \approx 0.8$, whereas it disappears at $y^+ \approx 100$. Comparing these results with the previous observations of a ZPG-TBL subjected to FST, where Dogan *et al.* [28] observed considerable effects on the distributions of all the fluctuating components by increasing the FST, reveals that the internal boundary layer shows greater robustness to the incoming turbulence conditions for the wall-normal fluctuations and Reynolds shear stress. Nonetheless, the streamwise
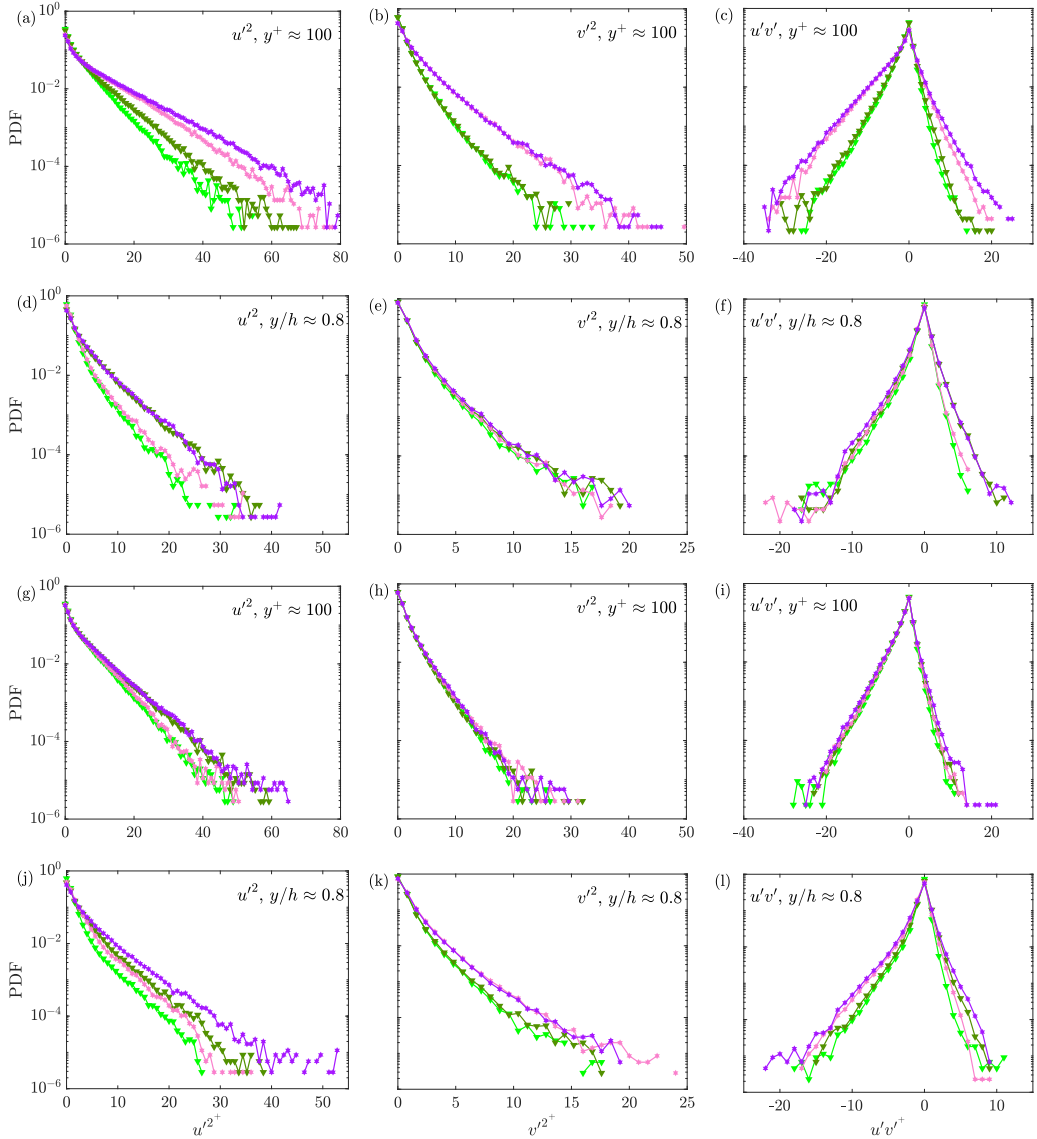
FIG. 9. Probability distribution functions (PDFs) of velocity fluctuations (u'^2, v'^2, and $u'v'$ in columns 1, 2, and 3, respectively) at two wall-normal locations, $y^+ \approx 100$ and $y/h \approx 0.8$. (a)–(f) Above the injection plate ($X = 76H$), and (g)–(l) downstream of the injection plate ($X = 87H$), for cases I0_REF and I0_C (▼, green), as well as I4_REF and I4_C (⋆, purple) with darkening colors indicating increased inlet turbulence intensity, i.e., REF and C, respectively.

fluctuations behave similarly in this paper and in that of Dogan *et al.* [28], i.e., the FST has a diminishing effect on the streamwise fluctuations as one approaches the wall.

To investigate the effects of localized injection, the highest injection cases are compared with the no-injection ones. On top of the injection plate ($X = 76H$) in the inner layer ($y^+ \approx 100$), all the Reynolds stress components are considerably affected by injection, and all the PDFs rise. Figure 9(a) demonstrates that, although the effect of the injection is dominant in the inner layer, the inlet turbulence effect is superimposed on top of it, which in turn yields even more extreme u' events.

A closer look at this figure reveals that, in the presence of the injection, the inlet turbulence effect on the tail of the PDF is propagated to even more extreme values. In contrast to the inner layer, the injection does not significantly affect the PDFs in the outer regions where the AL is absent. Farther downstream of the injection plate, i.e., $X = 87H$, the AL is transported to the outer region, and the inner layer of the boundary layer is recovered. Therefore, the injection effect is observed at $y/h \approx 0.8$ as raising the PDFs of all the Reynolds stress components, while the same effect does not exist at $y^+ \approx 100$ anymore, and the profiles roughly collapse for a given inlet turbulence intensity. It is evident that the injection effects are still present at this location, which is $>20h$ downstream of the injection zone.

B. Quadrant analysis

Turbulence-producing events in a boundary layer, i.e., $u'v' < 0$, can be classified into two categories: *sweep* events, where the fluid with high speed ($u' > 0$) is dragged toward the wall ($v' < 0$), and *ejection* events, where the fluid with low speed ($u' < 0$) is pushed away from the wall ($v' > 0$). The latter and the former correspond to the second quadrant (Q2) and fourth quadrant (Q4) in the u'-v' plane, respectively. The other two remaining motions correspond to positive correlations of $u'v'$ and are usually called *outward* ($u' > 0$ and $v' > 0$) and *inward* ($u' < 0$ and $v' < 0$) motions, corresponding to Q1 and Q3 in the u'-v' plane, respectively. Using the weighted joint PDF (JPDF) of streamwise and wall-normal fluctuations, the total Reynolds shear stress can be described as the sum of all these events as

$$\overline{u'v'} = \int_{-\infty}^{\infty} \int_{-\infty}^{\infty} u'v' f_{u,v}(u', v') \, du' dv', \tag{1}$$

where $u'v' f_{u,v}(u', v')$ is the weighted JPDF. Thus, contributions of different quadrant events can be evaluated by examining the weighted JPDF in the u'-v' plane. Accordingly, to examine the effects of the inlet turbulence and localized injection on Reynolds shear stress events, weighted JPDFs of the different test cases are presented in Fig. 10. In the inner region of the boundary layer at $y^+ \approx 100$, Q2 and Q4 events have the major contributions as expected for a boundary layer [50]. At $y^+ \approx 100$, the inlet turbulence enlarges the horizontal extent of the elliptical shapes in all the quadrants except for Q2 [Figs. 10(a), 10(b), 10(i), and 10(j)]. This effect is more prominent for Q4 events, indicating the penetration of the added turbulence into the inner region of the boundary layer, which in turn tends to equalize the Q2 and Q4 contributions to the total mean Reynolds shear stress. In the outer region at $y/h \approx 0.8$, the contributions of the quadrants are more balanced than in the inner region, and the effect of the inlet turbulence is more intense [Figs. 10(e), 10(f), 10(m), and 10(n)]. Nevertheless, the inlet turbulence still enlarges the distributions along the horizontal axis, indicating a neutral effect on the wall-normal fluctuations. This is a deviation from the previous observations by Dogan *et al.* [28], where the same analysis for a ZPG-TBL under the influence of FST showed that the weighted JPDFs are more circular in the outer regions, indicating impacts on both the streamwise and wall-normal fluctuations.

Focusing on injection, the created AL has a major impact on the weighted JPDFs above the injection zone ($X = 76H$) in the inner layer ($y^+ \approx 100$), where the contours for the injection cases are enlarged in all quadrants and over both axes [Figs. 10(c) and 10(d)]. Farther downstream at $X = 87H$, where the AL is transported away from the wall, there is no effect on the inner region [Figs. 10(k) and 10(l)], yet a minor effect is observed in the outer layer at $y/h \approx 0.8$ [Figs. 10(o) and 10(p)], in agreement with the previous observations in Secs. III and IV A. It is conspicuous that injection impacts are diminished at the downstream location $X = 87H$, especially for the increased inlet turbulence intensity.

Quadrant analysis can be extended to investigate the contributions of the intense $u'v'$ events in each quadrant and how they are affected by localized injection and inlet turbulence. This can be done through the hole filtering analysis, introduced by Willmarth and Lu [20], where the contributions of the Reynolds shear stress events are only accounted for if their magnitude is F times greater than the
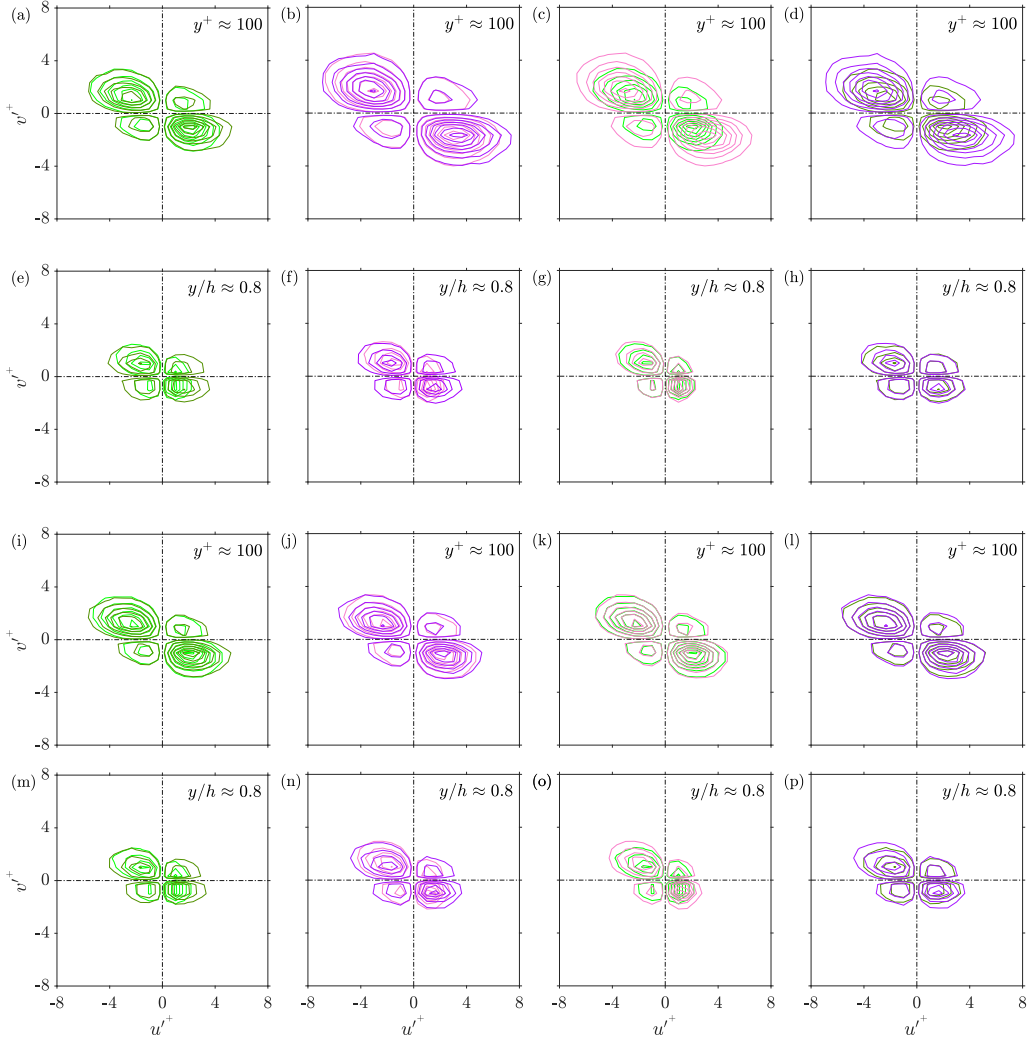
FIG. 10. Weighted joint probability density functions (JPDFs) of velocity fluctuations at two wall-normal locations, $y^+ \approx 100$ and $y/h \approx 0.8$. (a)–(h) Above the injection plate ($X = 76H$), and (i)–(p) downstream of the injection plate ($X = 87H$) for cases I0_REF and I0_C (light green and dark green, respectively), as well as I4_REF and I4_C (light purple and dark purple, respectively).

local mean value ($\overline{u'v'}$); here, F is a constant which acts as a threshold level. This can be formulated as

$$\frac{\langle u'v' \rangle|_{Q_i}}{\overline{u'v'}} = \frac{1}{\overline{u'v'}} \left(\frac{1}{N} \sum_{n=1}^{N} u'v'|_i A_i \right), \quad i = 1{:}4, \tag{2}$$

where N is the total number of samples, and A_i is defined as

$$A_i = \begin{cases} 1, & \text{when} |u'v'| \geqslant F |\overline{u'v'}|, \\ 0, & \text{otherwise.} \end{cases} \tag{3}$$

In this way, the Reynolds shear stress events inside a hyperbolic hole ($|u'v'| = F|\overline{u'v'}|$) in the u'-v' plane are discarded, and only the more intense events of each quadrant are averaged, indicating the
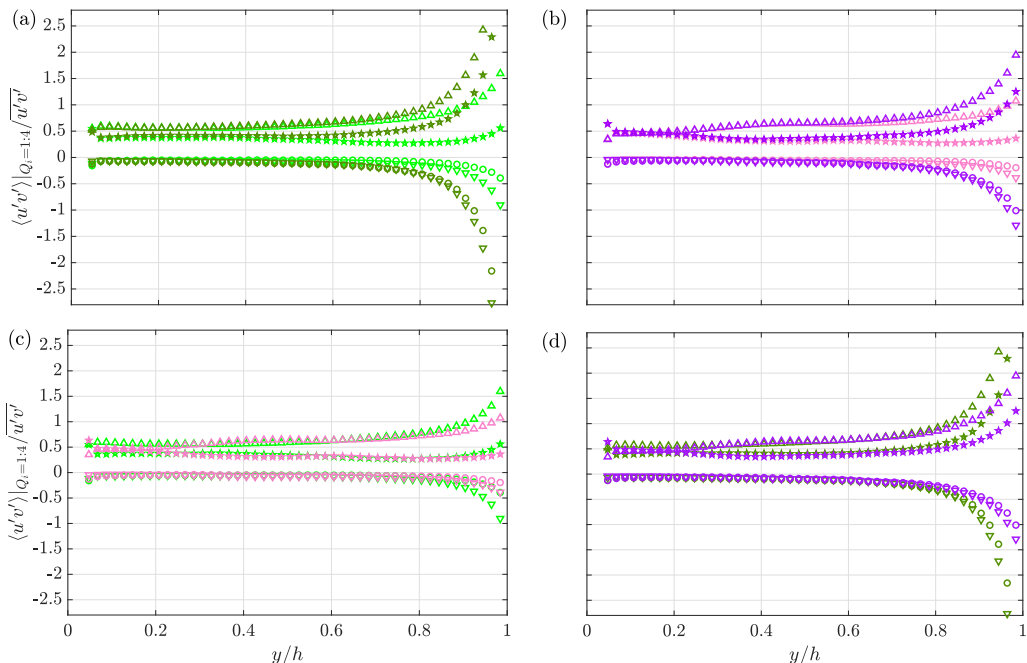
FIG. 11. Wall-normal distribution of intense quadrant contributions to the total Reynolds shear stress (Q1:○, Q2:△, Q3:▽, and Q4:☆) at $X = 76H$ for cases I0_REF and I0_C (light green and dark green, respectively), as well as I4_REF and I4_C (light purple and dark purple, respectively).

contribution of extreme shear events in each quadrant (see Wallace [51], Fig. 4 for visualization). Jiménez *et al.* [50] showed that, for a canonical channel flow, Q4 and Q2 events are the main contributors in the inner regions, with Q2 being slightly dominant. Moving to the outer regions, Q2 remains the dominant contributor; however, Q1 and Q3 contributions grow, compensating for the contributions of Q2 and Q4 events.

The results above the injection zone and farther downstream of it are shown in Figs. 11 and 12, respectively, for a constant value of $F = 1$. The penetration of the inlet turbulence slightly increases the contributions of intense Q4 events in the inner regions, yet Q2 remains dominant. For $y/h \gtrsim 0.4$, an increase in all the contributions of the extreme events is observed by increased inlet turbulence intensity. The effect increases in prominence as one moves toward the channel centerline, where the profiles diverge due to the vanishing total shear stress (the denominator of the ratios). Figures 11(c) and 11(d) show the effects of the injection across the AL ($y/h \lesssim 0.5$) on Q2 and Q4 events. These effects are opposite above and below the peak in the Reynolds shear stress profiles [Figs. 7(c) and 7(d)]. The contributions of Q2 and Q4 events are suppressed and amplified for $y/h \lesssim 0.2$, respectively, while the opposite is true for $0.2 \lesssim y/h \lesssim 0.5$. Also, Q3 events are totally blocked near the wall by localized injection. These notions are like the observations of Krogstad and Kourakine [14] regarding the effect of localized injection on a ZPG-TBL and are not considerably affected by the presence of added turbulence.

Farther downstream of the injection region, there is no interchange between the contributions of Q2 and Q4 events [Figs. 12(c) and 12(d)], as observed in the upstream position. Nevertheless, the contribution of Q2 is slightly decreased in locations around $y/h \approx 0.6$ by the AL, which is now transported away from the wall, and again, near the channel centerline, there is a mismatch for all the contributions due to the increased $\overline{u'v'}$ values.
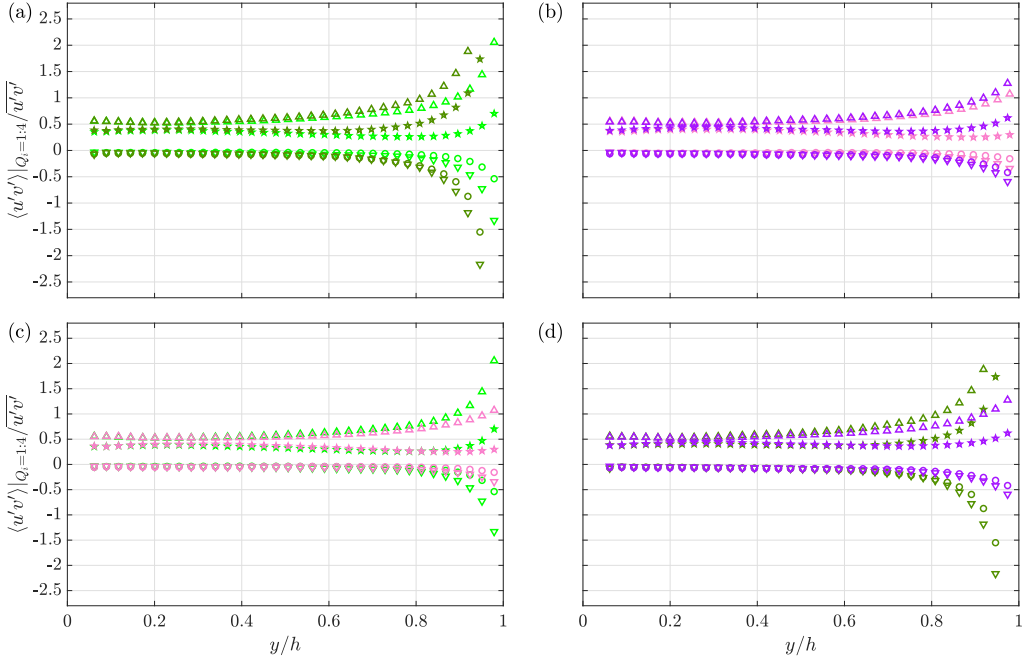
FIG. 12. Wall-normal distribution of intense quadrant contributions to the total Reynolds shear stress (Q1:○, Q2:△, Q3:▽, and Q4:☆) at $X = 87H$ for cases I0_REF and I0_C (light green and dark green, respectively), as well as I4_REF and I4_C (light purple and dark purple, respectively).

C. Correlations

Two-point spatial correlation analysis is performed to examine the effects of localized injection and inlet turbulence on the coherent structures of turbulent channel flow. Fixing the reference point, the two-point correlation coefficient is calculated for the streamwise fluctuations as

$$R_{u'u'} = \frac{\overline{u'(x, y)u'(x + \Delta x, y + \Delta y)}}{\sqrt{\overline{u'^2(x, y)}} \sqrt{\overline{u'^2(x + \Delta x, y + \Delta y)}}}, \tag{4}$$

where Δx and Δy are the spatial separations in the streamwise and wall-normal directions, respectively, and the overbar denotes ensemble-averaged over the multiple PIV fields. For conciseness, Fig. 13 shows the correlation contour lines only for some of the cases calculated at two different wall-normal locations ($y^+ \approx 100$ and $y/h \approx 0.8$). Figures 13(a) and 13(b) compare the I0 cases with different inlet turbulence conditions, indicating no significant effect on the shape of the structures. Despite the effects of FST on the coherent structures of ZPG-TBL [28], total robustness is observed here, which is related to the inherent difference between the internal and external boundary layers, where in a channel flow, the large-scale motions are set by geometry and are independent of inlet conditions. The same observations were made when comparing the I4 cases with different inlet conditions (not shown here). As seen in Fig. 13(c) for cases I0_C_76 and I4_C_76, the near-wall structures are slightly tilted, above the injection zone at $X = 76H$, in the presence of wall injection.

The same method as employed by Dogan *et al.* [28] is utilized here to estimate the inclination angle of the near-wall structures by fitting a rotated ellipse to the contour level $+0.25$. The inclination angle of the coherent structures is estimated as the rotation angle of the fitted ellipse. The resulting values are $13.7°$ and $16.6°$, for I0_REF_76 and I4_REF_76, respectively, estimated
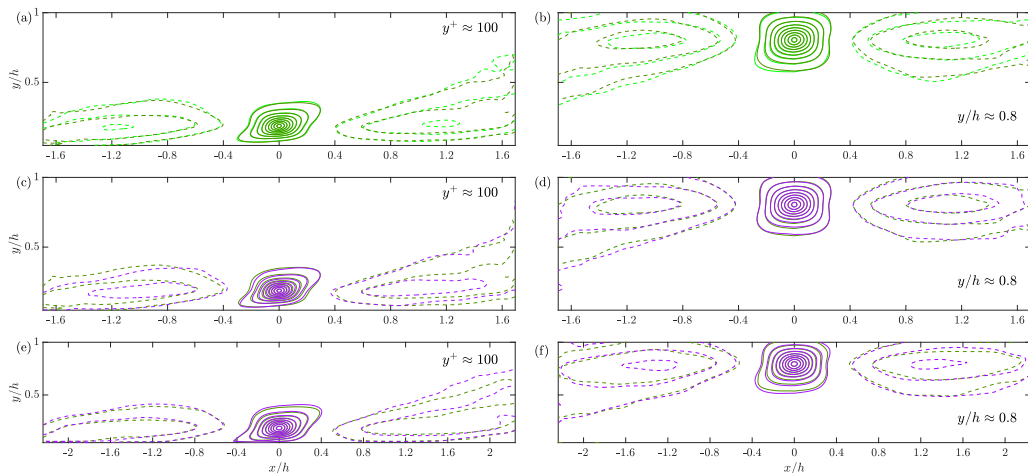
FIG. 13. Spatial two-point autocorrelation ($R_{u'u'}$) computed at (a)–(d) $X = 76H$ and (e)–(f) $X = 87H$ for cases I0_REF, I0_C, and I4_C (light green, dark green, and dark purple, respectively). The dashed lines show the negative contours. The outermost contour levels are 0.15 and -0.1, while the increments are 0.1 and -0.1 for positive and negative contours, respectively.

using the correlation contours at $y^+ \approx 100$. The former is like the value reported by Christensen and Adrian [52] for turbulent channel flow at $Re_\tau = 547$ (13°). Moreover, an increase in the inclination angle of the near-wall coherent structures by wall injection is in line with the previous observations of Haddad *et al.* [18]. The estimated inclination angles are slightly lower than that reported by Haddad *et al.* [18], which is like the observation of Dogan *et al.* [28], where the inclination angles estimated using PIV results were generally lower than that estimated by hot-wire data (see Dogan *et al.* [28], Fig. 16). The inclination angles reported above for the REF cases do not considerably change with increasing inlet turbulence, indicating that inlet turbulence does not play a significant role here. It is worth noting that the localized injection does not affect the total extension of the structures, demonstrating the robustness of the near-wall coherent structures of turbulent channel flow to external disturbances. The structures are unaffected in the outer region at $X = 76H$ [Fig. 13(d)]. However, farther downstream at $X = 87H$, where the AL is transported to the outer regions of the boundary layer, the structures are slightly stretched by the wall injection [Fig. 13(f)]. At this location, downstream of the injection zone, the near-wall structure is recovered, and the inclination angle is no longer affected by the upstream localized injection [Fig. 13(e)].

V. SUMMARY AND DISCUSSION

As illustrated in Fig. 14, an AL is created at the leading edge of the injection plate, which develops downstream. The localized injection influences the flow in the AL, where it decelerates the flow and amplifies both the normal and shear Reynolds stresses. In addition, the injection interchanges the contributions of the strong Q2 and Q4 events in the near-wall region by decreasing and increasing their contributions, respectively. The inclination angle of the near-wall structures also increases due to the injection.

In the outer regions, closer to the channel centerline, inlet turbulence plays a prominent role by suppressing the wake region of the velocity profile and increasing the streamwise fluctuations [Fig. 14]. Moreover, the inlet turbulence penetrates into the inner regions, where its impact on the streamwise fluctuations is superimposed onto the injection effects. Meanwhile, as illustrated in Fig. 14, the transport of the AL is enhanced in the presence of the added turbulence. The
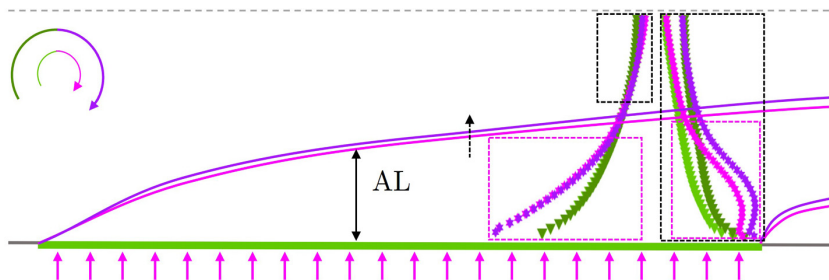
FIG. 14. Diagram of the simultaneous effects of inlet turbulence and wall injection on the streamwise statistics of the turbulent channel flow above the injection zone. The regions affected by the inlet turbulence and localized injection are indicated by black and purple dashed lines, respectively. The gray dashed line indicates the channel centerline.

near-wall structure of the channel shows a high degree of robustness to the inlet turbulence, as the contributions of the extreme quadrant events and the near-wall coherent structures remain untouched in the presence of the added turbulence.

Farther downstream of the injection zone, the strength of the injection effects is diminished. Nevertheless, the effects on the mean flow and Reynolds stresses are still traceable in the outer regions, where the AL resides at this downstream location.

Both injection and inlet turbulence primarily influence the streamwise fluctuations. One attempt to produce the combined effects of the injection and inlet turbulence would be to superimpose the inlet turbulence effect onto the injection effects. This idea is tested here by adding the difference in the streamwise fluctuations of cases I0_C_76 and I0_REF_76 to I2_REF_76, I3_REF_76, and I4_REF_76 cases to reconstruct the streamwise normal Reynolds stress profiles. Figure 15 compares the measured and reconstructed profiles. The eye is immediately drawn to the AL, where the superimposed profiles need to be slightly shifted to the right to compensate for the enhanced transport of the AL in the presence of increased inlet turbulence. Considering the uncertainty of the measurements, a linear superimposition reasonably reconstructs the measured profiles.

VI. CONCLUSIONS

The combined effects of localized wall injection and inlet turbulence on the structure of turbulent channel flow were examined by performing PIV measurements at two locations, above the injection zone and downstream of it. An active grid located at the inlet of the air channel was utilized to
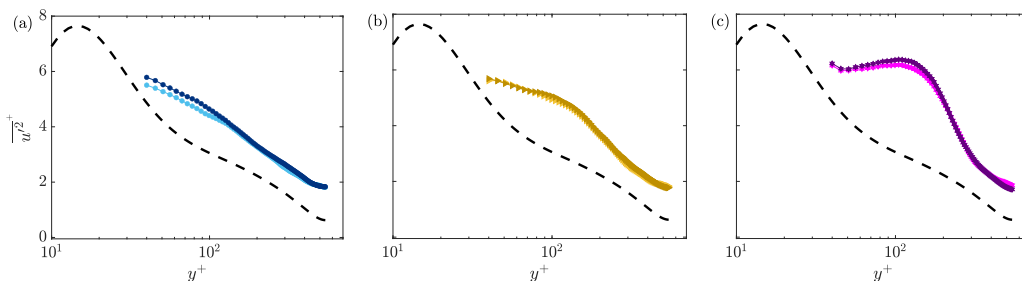
FIG. 15. The reconstructed (lighter colors) and measured (darker colors) inner-normalized streamwise normal Reynolds stress profiles for cases (a) I2_C_76, (b) I3_C_76, and (c) I4_C_76. The dashed black lines indicate DNS data of turbulent channel flow at $\mathrm{Re}_\tau \approx 550$ [49].

produce various inlet turbulence intensities. A pressurized injection chamber with a porous plate on top of it was embedded in the bottom wall of the channel to locally inject air streams with different injection rates. The experiments were carried out at $\text{Re}_H \approx 22\,300$, resulting in a matched $\text{Re}_\tau \approx 535$ for cases without the wall injection and indicating the same robustness of U_τ to the inlet turbulence level as observed by Asadi *et al.* [36]. The results show that the localized injection profoundly affects all the turbulence statistics, e.g., decreasing the mean velocity and increasing the turbulent fluctuations, across an AL, which is transported toward the outer regions moving downstream of the injection zone. However, the effects of increasing the inlet turbulence intensity are limited to a minor wake suppression and an increase in the streamwise fluctuations. The effects are almost superimposed when the localized injection and inlet turbulence are combined. As a result, the upward transport of the AL is enhanced due to the increased turbulence transport. Downstream of the injection plate, the near-wall structure of the channel flow recovers, and the effects of the injection are predominantly on the central region of the channel.

To further elaborate on the effects, turbulence structure analyses were performed in the inner and outer regions. It was confirmed by these analyses that the localized injection effects are mainly distributed across the AL, which resides in the near-wall region above the injection zone and moves to the outer regions farther downstream of the injection plate. The inlet turbulence mainly affects the outer regions of the boundary layer; nevertheless, traces of the penetrated turbulence are present in the inner regions. Moreover, PDF and JPDF analyses revealed that increasing inlet turbulence intensity does not significantly affect the structure of the wall-normal fluctuations and Reynolds shear stresses, in contrast to measurements in a ZPG-TBL. Nonetheless, increased turbulence intensifies the streamwise fluctuations, even in the inner regions of the boundary layer. Quadrant analysis revealed that the penetration of the inlet turbulence into the boundary layer increases the contributions of Q1, Q3, and Q4 events to the total shear stress in the inner regions, with the contributions of the Q2 events being untouched. The contributions of the extreme Reynolds shear stress events were intensified in the outer regions. Above the injection zone, in the near-wall region, strong Q4 events dominate in the presence of wall injection. Correlation analysis revealed that, in contrast to the previous notions of Dogan *et al.* [28] regarding the impact of FST on near-wall structures of ZPG-TBL, the inclined features of turbulent channel flow are independent of inlet turbulence intensity. The inclination angle of the near-wall structures increases with increasing injection rate, while their extent remains the same. These notions show that the large-scale structures of the channel are predominantly dictated by its geometry and are resilient to external perturbations.

The primary takeaway from this investigation is that, when considering the concurrent effects of localized wall injection and increased inlet turbulence on turbulent channel flow structure, incorporation of inlet turbulence was necessary since, despite a wide range of studies on canonical boundary layers subjected to wall injection, interactions of these two stimuli, i.e., localized injection and inlet turbulence, could not be known *a priori*.

APPENDIX: INVESTIGATION OF THE STREAMWISE GRADIENT FOR THE HIGHEST INJECTION CASE

As mentioned in Sec. III, the injection creates a strong streamwise gradient of the statistics above the injection plate, through which the AL is transported away from the wall. However, this process was masked by streamwise averaging of the PIV velocity fields and is elaborated on here by assessing the profiles at the upstream and downstream edges of the field of view. The highest injection cases with extreme turbulence levels, i.e., I4_REF_76 and I4_C_76, are investigated here
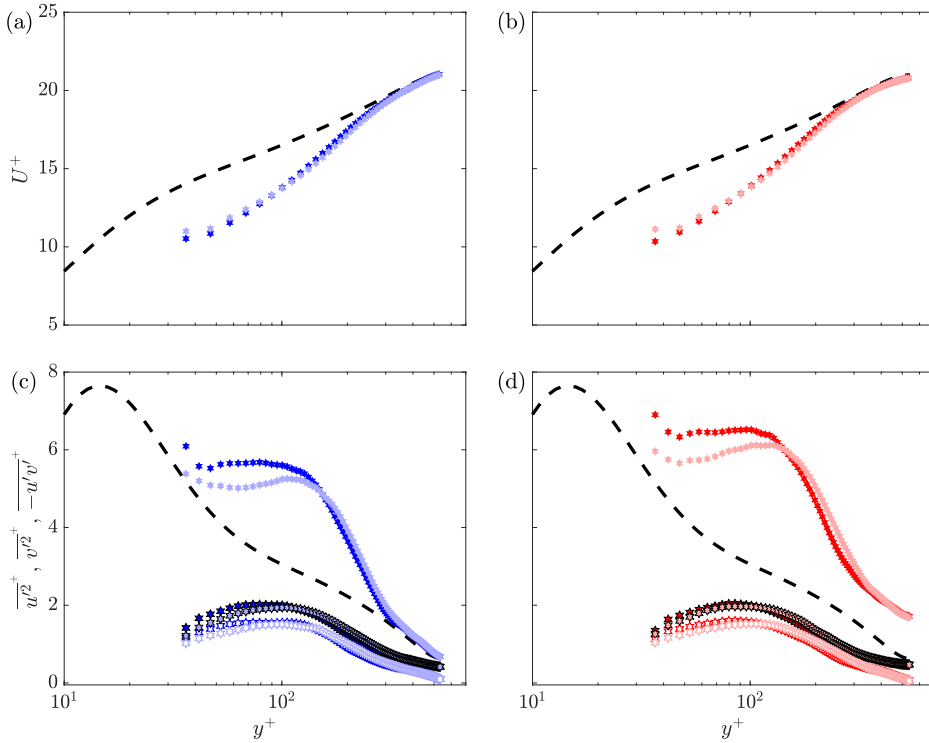
FIG. 16. Streamwise evolution of inner-normalized turbulence statistics for the highest injection rate, i.e., I4 at $X = 76H$. Mean velocity profiles for cases (a) REF and (b) C. Streamwise normal (filled symbols) and wall-normal (symbols with black border) Reynolds stresses, as well as Reynolds shear stress (open symbols) for cases (c) REF and (d) C. Darker and lighter colors show averaged profiles across $0 < x/h < 0.5$ and $1.2 < x/h < 1.7$, respectively. The dashed black lines indicate DNS data of turbulent channel flow at $Re_\tau \approx 550$ [49].

by averaging the statistics over the 2700 PIV fields. The resulting time-averaged fields were then averaged at the edges across a streamwise extent of $\sim 0.5h$. Figure 16 shows the resulting profiles of the mean velocity and turbulent fluctuations, where the effects of the injection spread away from the wall toward the outer layer. As a result, the impacts are diminished in the inner layer ($y^+ \lesssim 150$), and the profiles recover. Furthermore, comparing the profiles of cases REF and C, especially the streamwise normal Reynolds stress [Figs. 16(c) and 16(d)], reveals the enhanced transport of the injection effects in the presence of the added turbulence, where the profiles are more distinguished for the highest turbulent case. This effect is qualitatively represented in Fig. 17, where the enhanced
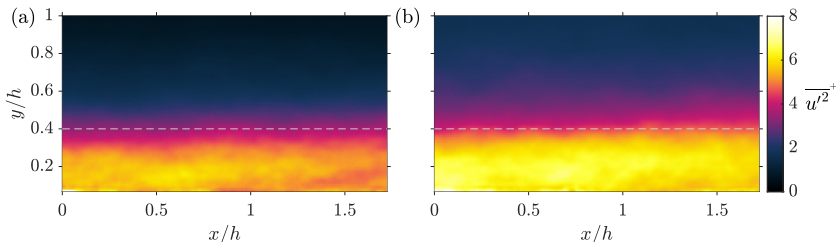
FIG. 17. Inner-normalized mean streamwise fluctuations fields in the lower half of the channel for cases (a) I4_REF_76 and (b) I4_C_76. The gray dashed lines show $y/h = 0.4$.

transport of the AL under the impact of increased inlet turbulence is evident by visual inspection, especially when compared with a horizontal reference line, e.g., $y/h = 0.4$.

[1] S. Dey and T. K. Nath, Turbulence characteristics in flows subjected to boundary injection and suction, J. Eng. Mech. **136**, 877 (2010).

[2] S. Dey, S. Sarkar, and F. Ballio, Double-averaging turbulence characteristics in seeping rough-bed streams, J. Geophys. Res.: Earth Surf. **116**, F03020 (2011).

[3] M. A. A. Faruque and R. Balachandar, Seepage effects on turbulence characteristics in an open channel flow, Can. J. Civ. Eng. **38**, 785 (2011).

[4] A. Singha, M. A. Al Faruque, and R. Balachandar, Vortices and large-scale structures in a rough open-channel flow subjected to bed suction and injection, J. Eng. Mech. **138**, 491 (2012).

[5] D. Cao, Y.-M. Chiew, and S.-Q. Yang, Injection effects on sediment transport in closed-conduit flows, Acta Geophysica **64**, 125 (2016).

[6] H. Choi, P. Moin, and J. Kim, Active turbulence control for drag reduction in wall-bounded flows, J. Fluid Mech. **262**, 75 (1994).

[7] E. Mori, M. Quadrio, and K. Fukagata, Turbulent drag reduction by uniform blowing over a two-dimensional roughness, Flow, Turbul. Combust. **99**, 765 (2017).

[8] M. Abbassi, W. Baars, N. Hutchins, and I. Marusic, Skin-friction drag reduction in a high-Reynolds-number turbulent boundary layer via real-time control of large-scale structures, Int. J. Heat Fluid Flow **67**, 30 (2017).

[9] X. Q. Cheng, Z. X. Qiao, X. Zhang, M. Quadrio, and Y. Zhou, Skin-friction reduction using periodic blowing through streamwise slits, J. Fluid Mech. **920**, A50 (2021).

[10] R. Baker and B. Launder, The turbulent boundary layer with foreign gas injection—I. Measurements in zero pressure gradient, Int. J. Heat Mass Transf. **17**, 275 (1974).

[11] J. A. Schetz and B. Nerney, Turbulent boundary layer with injection and surface roughness, AIAA J. **15**, 1288 (1977).

[12] M. Sano and N. Hirayama, Turbulent boundary layers with injection and suction through a slit: 1st report, mean and turbulence characteristics, Bull. JSME **28**, 807 (1985).

[13] J. Park and H. Choi, Effects of uniform blowing or suction from a spanwise slot on a turbulent boundary layer flow, Phys. Fluids **11**, 3095 (1999).

[14] P.-Å. Krogstad and A. Kourakine, Some effects of localized injection on the turbulence structure in a boundary layer, Phys. Fluids **12**, 2990 (2000).

[15] S.-H. Park, I. Lee, and H. J. Sung, Effect of local forcing on a turbulent boundary layer, Exp. Fluids **31**, 384 (2001).

[16] Y.-S. Park, S.-H. Park, and H. J. Sung, Measurement of local forcing on a turbulent boundary layer using PIV, Exp. Fluids **34**, 697 (2003).

[17] L. Keirsbulck, L. Labraga, and M. Haddad, Influence of blowing on the anisotropy of the Reynolds stress tensor in a turbulent channel flow, Exp. Fluids **40**, 654 (2006).

[18] M. Haddad, L. Labraga, and L. Keirsbulck, Turbulence structures downstream of a localized injection in a fully developed channel flow, J. Fluids Eng. **128**, 611 (2006).

[19] Y. Kametani, K. Fukagata, R. Örlü, and P. Schlatter, Effect of uniform blowing/suction in a turbulent boundary layer at moderate Reynolds number, Int. J. Heat Fluid Flow **55**, 132 (2015).

[20] W. Willmarth and S. Lu, Structure of the Reynolds stress near the wall, J. Fluid Mech. **55**, 65 (1972).

[21] M. F. Blair, Influence of free-stream turbulence on turbulent boundary layer heat transfer and mean profile development, part I—experimental data, J. Heat Transfer **105**, 33 (1983).

[22] P. E. Hancock and P. Bradshaw, The effect of free-stream turbulence on turbulent boundary layers, J. Fluids Eng. **105**, 284 (1983).

[23] P. E. Hancock and P. Bradshaw, Turbulence structure of a boundary layer beneath a turbulent free stream, J. Fluid Mech. **205**, 45 (1989).

[24] I. P. Castro, Effects of free stream turbulence on low Reynolds number boundary layers, J. Fluids Eng. **106**, 298 (1984).

[25] K. A. Thole and D. G. Bogard, High freestream turbulence effects on turbulent boundary layers, J. Fluids Eng. **118**, 276 (1996).

[26] N. S. Sharp, S. Neuscamman, and Z. Warhaft, Effects of large-scale free stream turbulence on a turbulent boundary layer, Phys. Fluids **21**, 095105 (2009).

[27] E. Dogan, R. E. Hanson, and B. Ganapathisubramani, Interactions of large-scale free-stream turbulence with turbulent boundary layers, J. Fluid Mech. **802**, 79 (2016).

[28] E. Dogan, R. J. Hearst, R. E. Hanson, and B. Ganapathisubramani, Spatial characteristics of a zero-pressure-gradient turbulent boundary layer in the presence of free-stream turbulence, Phys. Rev. Fluids **4**, 084601 (2019).

[29] R. J. Hearst, E. Dogan, and B. Ganapathisubramani, Robust features of a turbulent boundary layer subjected to high-intensity free-stream turbulence, J. Fluid Mech. **851**, 416 (2018).

[30] R. J. Hearst, C. M. de Silva, E. Dogan, and B. Ganapathisubramani, Uniform-momentum zones in a turbulent boundary layer subjected to freestream turbulence, J. Fluid Mech. **915**, A109 (2021).

[31] Y. Jooss, L. Li, T. Bracchi, and R. J. Hearst, Spatial development of a turbulent boundary layer subjected to freestream turbulence, J. Fluid Mech. **911**, A4 (2021).

[32] X. Wu, J. M. Wallace, and J.-P. Hickey, Boundary layer turbulence and freestream turbulence interface, turbulent spot and freestream turbulence interface, laminar boundary layer and freestream turbulence interface, Phys. Fluids **31**, 045104 (2019).

[33] J. You and T. A. Zaki, Conditional statistics and flow structures in turbulent boundary layers buffeted by free-stream disturbances, J. Fluid Mech. **866**, 526 (2019).

[34] J. You and T. A. Zaki, Turbulent heat-transfer enhancement in boundary layers exposed to free-stream turbulence, Flow, Turbul. Combust. **104**, 381 (2020).

[35] M. Kozul, R. J. Hearst, J. P. Monty, B. Ganapathisubramani, and D. Chung, Response of the temporal turbulent boundary layer to decaying free-stream turbulence, J. Fluid Mech. **896**, A11 (2020).

[36] M. Asadi, M. Kamruzzaman, and R. J. Hearst, The effect of inlet turbulence on the quiescent core of turbulent channel flow, J. Fluid Mech. **935**, A37 (2022).

[37] M. A. Miller, A. Martin, and S. C. C. Bailey, Investigation of the scaling of roughness and blowing effects on turbulent channel flow, Exp. Fluids **55**, 1675 (2014).

[38] C. G. Borchetta, A. Martin, and S. C. C. Bailey, Examination of the effect of blowing on the near-surface flow structure over a dimpled surface, Exp. Fluids **59**, 36 (2018).

[39] A. M. Hamed, C. E. Nye, and A. J. Hall, Effects of localized blowing on the turbulent boundary layer over 2D roughness, Exp. Fluids **62**, 163 (2021).

[40] Y. Marchenay, F. Chedevergne, and M. Olazabal Loumé, Modeling of combined effects of surface roughness and blowing for Reynolds-averaged Navier–Stokes turbulence models, Phys. Fluids **33**, 045116 (2021).

[41] J. P. Monty, Developments in smooth wall turbulent duct flows, Ph.D. thesis, University of Melbourne, 2005.

[42] R. Vinuesa, A. Noorani, A. Lozano-Durán, G. K. E. Khoury, P. Schlatter, P. F. Fischer, and H. M. Nagib, Aspect ratio effects in turbulent duct flows studied through direct numerical simulation, J. Turbul. **15**, 677 (2014).

[43] R. Vinuesa, P. Schlatter, and H. M. Nagib, Secondary flow in turbulent ducts with increasing aspect ratio, Phys. Rev. Fluids **3**, 054606 (2018).

[44] K. A. Flack, M. P. Schultz, and W. B. Rose, The onset of roughness effects in the transitionally rough regime, Int. J. Heat Fluid Flow **35**, 160 (2012).

[45] J. V. Larssen and W. J. Devenport, On the generation of large-scale homogeneous turbulence, Exp. Fluids **50**, 1207 (2011).

[46] R. J. Hearst and P. Lavoie, The effect of active grid initial conditions on high Reynolds number turbulence, Exp. Fluids **56**, 185 (2015).

[47] A. Sciacchitano, D. R. Neal, B. L. Smith, S. O. Warner, P. P. Vlachos, B. Wieneke, and F. Scarano,

Collaborative framework for PIV uncertainty quantification: comparative assessment of methods, Meas. Sci. Technol. **26**, 074004 (2015).

[48] B. Wieneke, PIV uncertainty quantification from correlation statistics, Meas. Sci. Technol. **26**, 074002 (2015).

[49] M. Lee and R. D. Moser, Direct numerical simulation of turbulent channel flow up to $Re_\tau \approx 5200$, J. Fluid Mech. **774**, 395 (2015).

[50] J. Jiménez, S. Hoyas, M. P. Simens, and Y. Mizuno, Turbulent boundary layers and channels at moderate Reynolds numbers, J. Fluid Mech. **657**, 335 (2010).

[51] J. M. Wallace, Quadrant analysis in turbulence research: history and evolution, Annu. Rev. Fluid Mech. **48**, 131 (2016).

[52] K. T. Christensen and R. J. Adrian, Statistical evidence of hairpin vortex packets in wall turbulence, J. Fluid Mech. **431**, 433 (2001).